

Experimental and numerical investigation of a micro-CHP flameless unit

A. Parente ^a, C. Galletti ^b, J. Riccardi ^c, M. Schiavetti ^c, L. Tognotti ^{b,*}

^a Service d'Aéro-Thermo-Mécanique, Université Libre de Bruxelles, Bruxelles, Belgium

^b Dipartimento di Ingegneria Chimica, Chimica Industriale e Scienza dei Materiali, Università di Pisa, Pisa, Italy

^c ENEL Ingegneria e Innovazione S.p.A., Area Tecnica Ricerca, Pisa, Italy

ARTICLE INFO

Article history:

Received 31 March 2010

Received in revised form 23 June 2011

Accepted 24 June 2011

Available online 24 August 2011

Keywords:

Flameless

Stirling cycle

Hydrogen

Combustion model

Kinetic mechanism

NO_x

ABSTRACT

A numerical and experimental investigation of a system for the micro-cogeneration of heat and power, based on a Stirling cycle and equipped with a flameless burner, is carried out with the purpose of evaluating the system performances with hydrogen-enriched fuels. The numerical model of the combustion chamber gave significant insight concerning the analysis and interpretation of the experimental measurements; however it required considerable efforts, especially regarding the definition of proper boundary conditions. In particular a subroutine was developed in order to couple the oxidation process to the overall operation of the micro-cogeneration unit. This procedure was proved to perform satisfactory, providing values of the heat source for the Stirling cycle that lead to expected thermal efficiencies in agreement with those indicated in the literature for similar systems. The importance of a proper turbulence-chemistry interaction treatment and rather detailed kinetic schemes to capture flameless combustion was also assessed. A simple NO formation mechanism based on the thermal and prompt routes was found to provide NO emissions in relatively good agreement with experimental observations when applied on thermo-fluid dynamic fields obtained from detailed oxidation schemes.

© 2011 Published by Elsevier Ltd.

1. Introduction

Combined heat and power generation (CHP), or cogeneration, has recently received particular attention as an alternative to conventional methods of producing heat and electricity separately.

In particular, the continuous fluctuations in energy price and the uncertainty in fuel supplies have determined a growing interest for the use of micro-cogeneration in the residential sector. In fact, micro-CHP systems are characterized by very high conversion efficiencies (over 80%) with respect to fossil fuel fired electricity generation systems. Moreover, distributed generation in decentralized systems is very appealing to reduce greenhouse gases emissions and to exploit the new opportunities offered by alternative fuels, such as hydrogen-based fuels obtained from biomass (and coal) thermal conversion processes.

Onovwiona and Ugursal [1] recently carried out a literature review on residential cogeneration systems, taking into account four different technologies: reciprocating internal combustion engines, micro-turbines, fuel cells and Stirling engines. The authors discussed the development stage of the technologies, indicating environmental benefits, performances and installation costs. As a result, the privileged choice for residential application appeared

to be the reciprocating internal combustion engines (ICE), due to their robustness, reliability and reasonable costs. However, the "maturity" of the ICE technology is also responsible of the poor performances of such systems from the environmental point of view, e.g. CO and NO_x emissions, although improvements have been recently made for micro-CHP applications [2]. On the other hand, innovative technologies such as Stirling engines are characterized by emissions about 10 times smaller [1] than those of Otto engines with catalytic converters and they offer more flexibility from the point of view of fuel nature.

A recent life cycle assessment [3] analysis on micro-cogeneration has indicated micro-CHP systems are superior in terms of GHG emissions to both average electricity and heat supply as well as to separate production of electricity in gas power plants and heat in condensing boilers. Among the existing possibilities (i.e. fuel cells, micro-turbines), cogeneration systems based on Stirling cycles appear particularly appealing, as they ensure high efficiency, fuel flexibility, low emissions, low noise/vibration levels and good performance at partial load [1]. Since the combustion process takes places outside the engine, different fuels may be used; moreover the combustion process can be controlled independently from the engine operation. Besides, the maintenance of Stirling engines is less critical compared to other reciprocating internal combustion engines, because of fewer moving parts leading to quieter and smoother operations. The versatility regarding the fuel topology is extremely important as it implies that non conventional fuels such as biomasses and low-calorific gases enriched with hydrogen could

* Corresponding author. Address: Dipartimento di Ingegneria Chimica, Chimica Industriale e Scienza dei Materiali, Università di Pisa, via Diotisalvi 2, I-56126 Pisa, Italy. Tel.: +39 050 2217840; fax: +39 050 2217866.

E-mail address: l.tognotti@diccsm.unipi.it (L. Tognotti).

Nomenclature

CI	confidence interval	ΔT_{\max}	maximum temperature rise, K
C_p	specific heat, $\text{J kg}^{-1} \text{K}^{-1}$	ε_{AIR}	air excess
\bar{E}	error associated to the numerical simulations	ε	kinetic energy dissipation rate, $\text{m}^2 \text{s}^{-3}$
F_s	safety factor	$\eta_{th,St}$	thermal efficiency of the Stirling engine
GCI	Grid Convergence Index	η_{reg}	regenerator efficiency
k	turbulent kinetic energy, $\text{m}^2 \text{s}^{-2}$	v	degrees of freedom
k_R	recirculation degree		
h	grid spacing, m		
n	number of experimental replicates		
\dot{m}	mass flow rate, kg s^{-1}		
P_{He}	helium operating pressure, Pa		
\dot{Q}_{rem}	heat removed in the flue gases/helium heat exchanger, W		
\dot{Q}_{in}	burner input power, W		
\dot{Q}_{air}	air preheating power, W		
\dot{Q}_{fg}	power recoverable from the exhaust gases, W		
r	radial coordinate, m		
r_{hc}	grid coarsening ratio		
r_{hf}	grid refining ratio		
s	sample standard deviation		
T	temperature, K		
$t_{z/2,v}$	quantile of the measured population		
x	axial coordinate, m		
y_m	predicted variable		
\bar{y}_e	measured variable		
Y	mass fraction		
U_e	experimental uncertainty		
U_{sver}	solution uncertainty		
W_{el}	electric power, W		
<i>Greek symbols</i>			
α	desired level of confidence		
<i>Subscripts</i>			
0	at ambient conditions		
air	air		
b	base grid		
c	coarse grid		
e	electrical		
f	fine grid		
g	flue gases		
g,R	recirculating flue gases		
$fuel$	fuel		
k	species index		
m	mixed value, referred to the mixing process of fresh and flue gases		
out	value at chimney		
th	thermal		
tot	overall		
<i>Abbreviations</i>			
BC	boundary condition		
CHP	combined heat and power generation		
EDC	Eddy dissipation concept		
HITAC	high temperature air combustion		
MILD	moderate or intense low-oxygen dilution		
PDF	probability density function		
WSGG	weighted sum of gray gases		

be effectively exploited, without damaging the engine. Indeed, the performances of the combustion system in terms of efficiency and pollutants emissions need to be assessed when working with non conventional fuels.

Thomas [4] recently performed a benchmark testing of four micro-CHP units in the range of 5–9 kW electric power, two of them based on Stirling engines and two Otto CHP units. The systems were compared on the basis on the German environmental regulation which fixes the admissible performances of CHP systems from the point of view of electrical, thermal and overall efficiencies, NO_x and CO emissions. Results of the benchmark clearly showed that the only unit able to meet all the regulation requirements was a SOLO Stirling unit [5], equipped with a flameless burner.

The implementation of flameless burners in micro-CHP units represents a very attractive solution, due to the great potentials of the flameless technology to deal with complex fuels. Flameless combustion [6], or MILD [7,8] of HITAC [9–11] has received particular attention in the last years due to its ability of combining high combustion efficiencies with extremely low pollutant emissions. Such combustion regime is based on the modification of the traditional flame structure: the system is driven towards homogeneous (temperature and species) conditions, by means of a massive recirculation of exhaust gases in the reaction region. As a result, the system approaches perfectly stirred reactor conditions and temperature increase due to combustion is diluted over a wider reaction zone. The volumetric nature of the combustion process allows achieving very high combustion efficiencies ensuring near zero CO emissions in the exhausts. Moreover, NO_x emissions are largely suppressed, even when large air preheating is applied, because of the reduced temperature peaks.

The latter effect appears particularly beneficial for controlling NO_x formation and shows potentials for limiting the reactivity of hydrogen-based fuels. The effectiveness of flameless combustion with hydrogen-based fuels has been recently demonstrated [11–15].

The present paper aims at investigating a flameless system for the micro-CHP of heat and power based on a Stirling cycle, with the purpose of evaluating its performance with hydrogen-enriched fuels. A joint experimental and modeling activity has been carried out to gain insight into the main features of the system, which shows complex geometry, due to its industrial characteristics, and operation, due to the coupling between the combustion process and a Stirling cycle. The available experimental data are, then, crucial for a constructive validation of the computational approach, with particular attention to oxidation kinetic schemes and pollutant formation models.

2. The burner

The investigated micro-CHP system¹ [5], is able of providing 2–9 kW of electricity and 22–30 kW of thermal power, with an electrical efficiency of 22–24% and a total efficiency larger than 90%. The system is equipped with a flameless burner for the oxidation of the gaseous fuel and a finned heat exchanger is placed inside the combustion chamber to supply power to a Stirling cycle operated with a different medium (i.e. helium). The CHP unit is designed to burn

¹ SOLO Stirling 161 Cogeneration Unit by SOLO® installed at the ENEL Ricerca facilities of Livorno, Italy.

natural gas; however the burner behavior with H₂ based fuels was studied varying the H₂ mass fraction in the fuel up to 10%.

The system consists of several sub-assemblies enclosed by an overall housing. The cylindrical and horizontally arranged combustion chamber (0.31 m long) is closed at the end and delimited by an external (steel) case with a diameter varying from 0.021 to 0.0235 m. Inside the combustion chamber, there is a flame tube (Fig. 1a) with a diameter of 0.087 m, into which fresh air and fuel are fed, and produce the oxidation process. The flue gases flow along the chamber axis until they reach the closed end and reverse direction, where the external enclosure diameter is larger. Then, the exhausts cross the finned heat exchanger, denoted as heater (Fig. 1a), which supplies heat to a helium stream carrying out a Stirling cycle. Finally, a part of exhaust gases is entrained into the flame tube by the incoming air, fed to the combustion chamber through six nozzles inclined by 25° with respect to the horizontal (Fig. 1b). The high momentum air jet also entrains the fuel, which is injected at low velocity through six nozzles inclined by 65° with respect to the horizontal (Fig. 1b). The recirculation of the flue gases into the reaction region is essential to achieve flameless combustion, as it ensures the dilution of the fresh gases as well as their preheating above the fuel self ignition temperature. The fraction of exhausts which do not recirculate in the reaction zone leaves the combustion chamber, crossing a honeycomb heat exchanger for air preheating. This allows increasing the overall efficiency, providing air at about 823 K. Before the chimney, exhaust gases are cooled down in a water–water heat exchanger. An additional

water–water heat exchanger is also included in the micro-CHP system, to recover the heat released by helium. The overall operation of the micro-CHP system with the main fluid streams and the heat exchanges is shown in Fig. 2. The system performances can be adjusted by varying the helium working pressure in the range 40–150 bar, corresponding to an electrical output from 2 to 9 kW.

Regarding the experimental measurements available, five thermocouples are placed on the external surface of the exhausts/helium heat exchanger to measure the flue gas temperature; moreover, the temperatures on top of the expansion cylinder of the Stirling cycle and before the chimney are also monitored. As for the species composition, the composition of the exhaust stream leaving the combustion chamber is characterized (O₂, CO₂, CO and NO).

2.1. Stirling engine

As mentioned previously, the finned heat exchanger (Fig. 1) provides heat to helium, which drives a Stirling engine (Fig. 2) for the generation of electrical power. The Stirling engine consists of a compression and an expansion cylinders, placed at 90°. Heater, regenerator and gas cooler are positioned between the two cylinders. The working gas is moved between the cylinders, undergoing a closed thermodynamic cycle. Inside the compression cylinder the gas is isothermally compressed at low temperature by water cooling; then, it is moved through a regenerator towards the expansion cylinder. The regenerator, hot in this case, heats the helium stream at temperature levels of about 923 K. During the isothermal

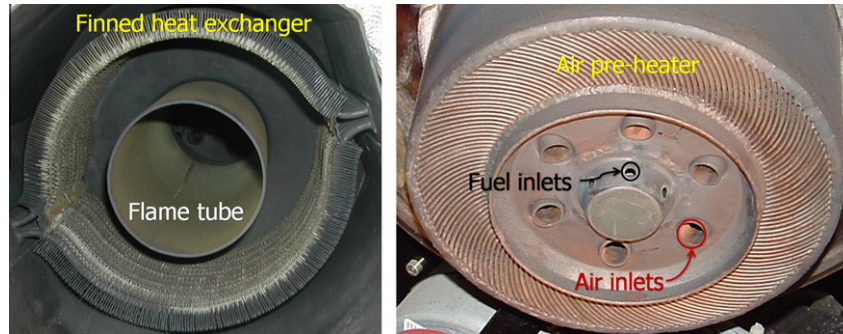


Fig. 1. Flame tube and finned heat exchanger (a); air and fuel feeding system (b).

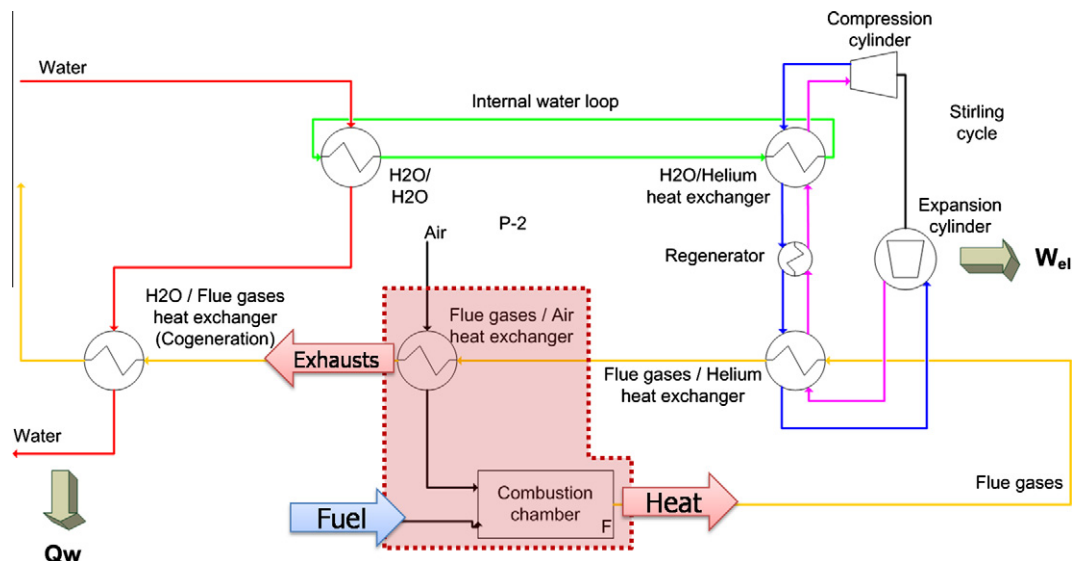


Fig. 2. Schematic diagram of flow streams and heat exchanges with highlighted combustion section.

expansion the gas is constantly heated by the heater; afterwards, the gas is moved back through the regenerator (cold in this case), where it is cooled down, to the compression cylinder. The use of a regenerator considerably improves the cycle efficiency.

3. Experimental campaign

The experimental campaign of the micro-CHP Stirling unit has been carried with different operating conditions, varying the hydrogen content in the fuel stream and the operating pressure of helium. Table 1 reports the boundary conditions for the experimental runs, whereas the main experimental results are listed in Table 2. Columns 2–5 in Table 2 list the composition of the flue gases for the different investigated runs. It can be observed that oxygen content in the flue gases increases with the hydrogen mass fraction. This is expected as the normal operation of the system leads to larger air excess for hydrogen-enriched mixtures, as indicated in Table 1. In addition CO and CO₂ levels decrease with H₂, because of the lower relative carbon fraction in the fuel. Finally, regarding NO emissions, a slight decrease is observed with increasing H₂, for higher burner loads (i.e. helium pressures, P_{He} , of 90 and 120 bar). This is due to the increase of air excess when hydrogen is added to the fuel, which leads to a higher dilution of the flue gases.

Table 1
Summary of the experimental campaign on the the CHP unit.

Run	\dot{m}_{NG} (kg/s)	\dot{m}_{H_2} (kg/s)	Y_{H_2} (–)	ε_{AIR} (%)	\dot{Q}_{in} (kW)	P_{He}
1	5.23E-04	0	0	48	26.1	90
2	4.47E-04	3.14E-05	0.07	73	26.2	90
3	4.42E-04	4.34E-05	0.09	82	27.3	90
4	6.39E-04	0	0	43	32.0	120
5	5.62E-04	3.97E-05	0.07	69	32.9	120
6	5.37E-04	5.62E-05	0.09	79	33.6	120

Columns 6–10 of Table 2 summarize the performances of the system at the investigated conditions. The electrical, \dot{W}_{el} , and thermal power, \dot{Q}_{th} , are listed, together with the efficiencies (electric, η_e , thermal, η_{th} , and overall, η_{tot}). It can be observed how all the efficiencies rise with the burner load, i.e. helium pressure, reaching values around 97–98%. At lower burner loads the system performances are lower, as expected, because the system operates in off-design conditions and the influence of the heat losses is more significant.

4. Numerical modeling of the micro-CHP flameless unit

The numerical modeling of the Stirling CHP unit has been carried out with the commercial software FLUENT 6.3 by Ansys Inc.

The activity has been focused on the combustion section of the system. Hypotheses regarding the overall operation of the micro-CHP unit have been made to determine the heat exchange between the flue gases and the operating fluid, i.e. helium, of the Stirling cycle. The following sections describe the approach adopted, which is also summarized in the scheme of Fig. 3.

4.1. Computational domain and grid

The geometry of the combustion chamber is rather complex, due to the presence of six injection nozzles for both air and fuel streams (Fig. 4). Moreover, a detailed description of the flue gases/helium heat exchanger (Fig. 1a) is not feasible, due to the large number of grid cells that would be required to model the geometrical details of the heater. Simplifications need to be made, to minimize the impact of the mesh on the overall computational resources, while ensuring an acceptable accuracy in the representation. Following the above considerations, it has been chosen to model a 60° angular section of the real combustion chamber. The

Table 2
Flue gas composition (dry basis) and main operation outputs for the runs investigated in Table 1.

Run	CO (ppm _v)	NO (ppm _v)	O ₂ (% vol)	CO ₂ (% vol)	\dot{W}_{el} (kW)	\dot{Q}_{th} (kW)	η_e (–)	η_{th} (–)	η_{tot} (–)
1	12.0	50.5	6.4	8.1	7.0	17.0	0.65	0.27	0.92
2	6.2	45.6	8.5	6.1	7.2	17.6	0.67	0.28	0.95
3	5.9	45.8	7.8	6.7	7.3	17.8	0.65	0.27	0.92
4	17.4	49.0	5.9	8.3	9.1	22.0	0.69	0.28	0.97
5	7.9	40.8	8.0	6.4	9.1	23.0	0.70	0.28	0.98
6	6.6	39.0	8.6	5.8	9.1	23.5	0.70	0.27	0.97

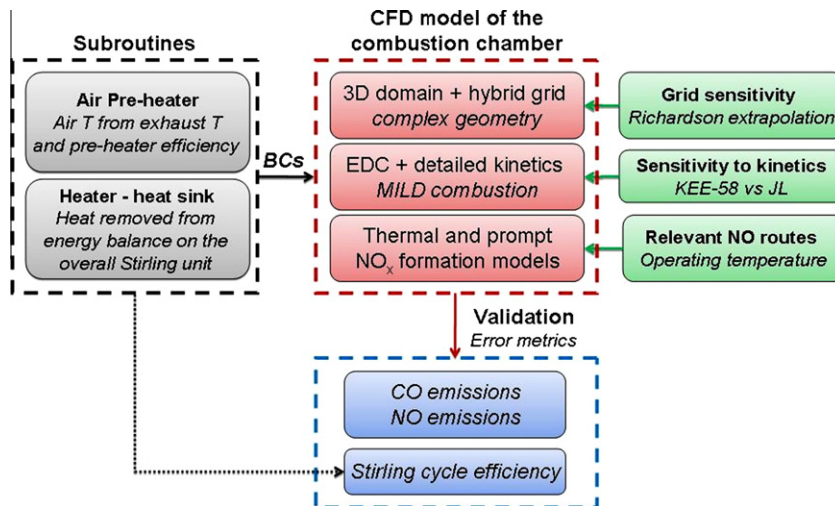


Fig. 3. Scheme of the modeling approach.

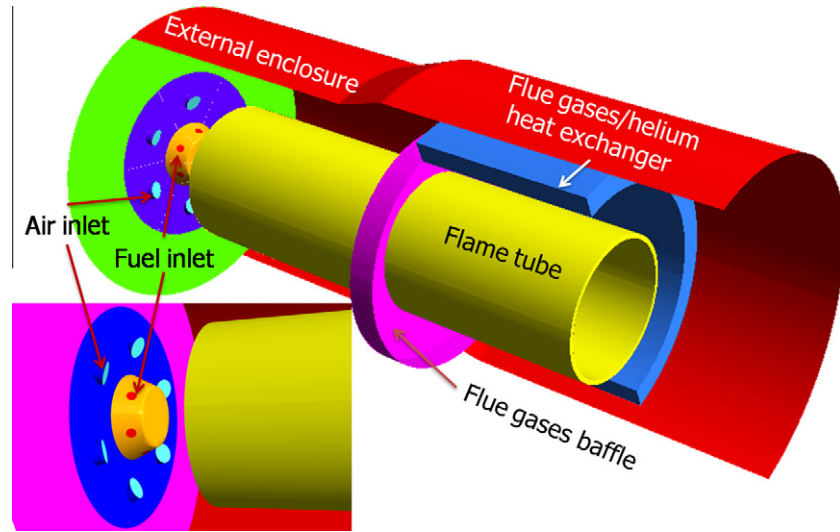


Fig. 4. Sketch of the combustion chamber and details about the feeding system.

heat exchanger has been treated as a fluid sub-domain with a heat sink equal to the heat transferred from the flue gases to helium. Details about the calculation of the heat removed by the heater are given in Section 4.2. Finally, the flame tube (Fig. 1a) has been modeled as a solid domain placed inside the combustion chamber.

A hybrid approach has been adopted to reduce the overall number of computational cells (Fig. 5). For the fluid domain, a hexahedral mesh has been used everywhere with the exception for the injection region, where a tetrahedral mesh is preferred to reproduce accurately injection nozzles. The air and injection nozzles have been extended upstream the nozzles of about five characteristic diameters, to ensure the flow to be fully developed at the burner exit plane. The cell size is not uniform and a higher density is

observable in the injection region, to provide a better characterization of the reaction structure. The flame tube is also meshed with hexahedra. The resulting total number of cells for the base mesh is about 382.000. A grid sensitivity analysis has been carried out to estimate the solution error associated to the discretization adopted. To this purpose, two additional grids have been taken into account, a finer and a coarser one. The finer grid has been obtained by applying a uniform refining ratio, i.e. $r_{hf} = h_f/h_b = 0.8$, to the base mesh, in axial and radial directions. Similarly, the coarser grid is obtained by applying a constant coarsening factor $r_{hc} = h_c/h_b = 1.25$ to the base mesh. The total number of grid cells for the finer and coarser grid is 550.000 and 270.000, respectively. The meshes have been compared in a cold flow simulation, with boundary

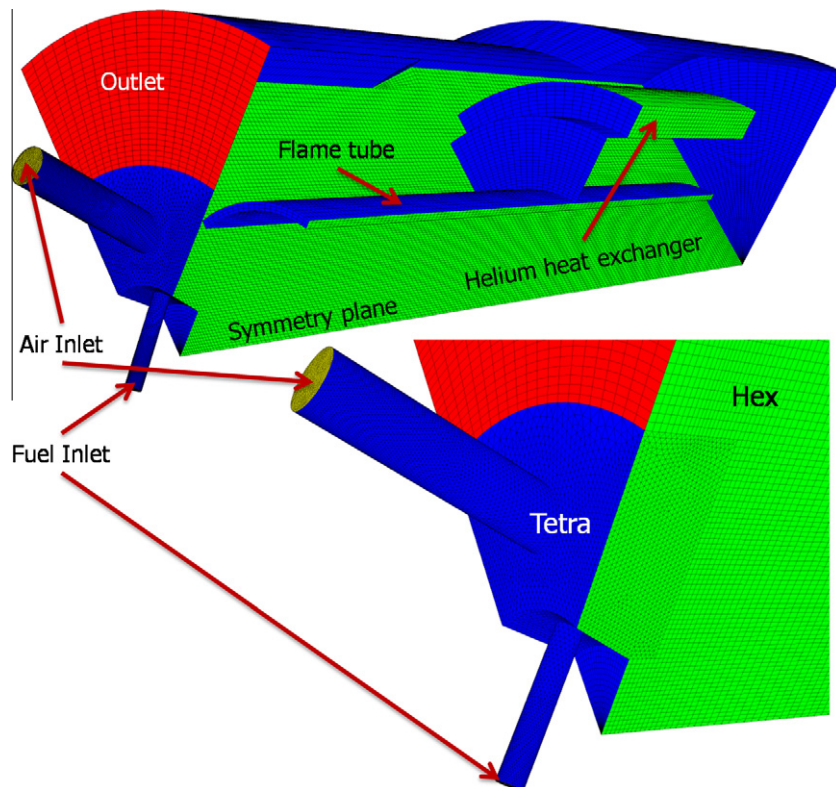


Fig. 5. Computational domain and grid with details of the injection nozzles.

conditions taken from run 4 in Table 2. A solution uncertainty, U_{sver} , has been estimated following Logan and Nitta approach [16]. The Grid Convergence Index (GCI) has been also estimated, assuming a safety factor, $F_s = 1.25$, as advised by Roache [17] for a set of three meshes. Table 3 lists the values of U_{sver} and GCI for the set of investigated meshes. The values have been obtained by averaging the radial profiles of axial velocity within the flame tube. Table 3 clearly indicates values of U_{sver} and GCI for the base grid below 5–7%, which can be considered a reasonable compromise between CPU time requirements and the numerical accuracy.

4.2. Boundary conditions

As far as boundary conditions (BCs) are concerned, mass flow rate BCs are used to specify the inlets. Fuels, i.e. methane and hydrogen, are fed at room temperature whereas air temperature downstream of the pre-heater is not known from the experimental measurements. Therefore, it has been evaluated from the exhaust gas temperature by assuming a preheating efficiency of 50%. Such value ensures a preheating temperature of about 823 K for nominal operating conditions, with the burner fed with natural gas and a helium pressure of 120 bar, as indicated by the burner manufacturer [5].

An user-defined subroutine has been developed to model the heat exchanger behavior and to estimate the air inlet temperature (Fig. 3). The heater is modeled as a fluid domain with a heat sink. Therefore, the external subroutine performs an energy balance on the overall unit to determine the heat removed by the exhaust stream. In particular, the following operations are performed:

1. The average temperature of the exhaust gases is calculated, by averaging the temperatures of each cell adjacent to the outlet boundary condition.
2. Assuming a preheating efficiency equal to 50%, the air inlet temperature is estimated from the exhaust gas temperature.
3. The heat recoverable from the exhaust gases, \dot{Q}_{fg} , and the air preheating heat, \dot{Q}_{air} , are calculated, given the flue gas temperature at the chimney, $T_{fg,out}$, and the ambient air temperature, $T_{air,0}$, known from the experimental campaign (Table 1).

$$\begin{aligned}\dot{Q}_{fg} &= \dot{m}_{fg} c_{p,fg} (\bar{T}_{fg}) (T_{fg} - T_{fg,out}) \\ \dot{Q}_{air} &= \dot{m}_{air} c_{p,air} (\bar{T}_{air}) (T_{air} - T_{air,0})\end{aligned}\quad (1)$$

where $c_{p,fg} (\bar{T}_{fg})$ and $c_{p,air} (\bar{T}_{air})$ are the specific heat at constant pressure calculated at average flue and air temperatures, respectively. The coefficients for the evaluation of the specific heat are taken from the CHEMKIN Thermodynamic Database [18].

4. An energy balance is carried out on the control region indicated in Fig. 2, to determine the heat transferred from the flue gases to helium in the combustion chamber. Then, the heat removed in the flue gases/helium heat exchanger, \dot{Q}_{rem} , is:

$$\dot{Q}_{rem} = \dot{Q}_{in} - \dot{Q}_{fg} + \dot{Q}_{air} \quad (2)$$

where \dot{Q}_{in} is the thermal input, known from the experimental campaign (Table 1).

5. The heat, \dot{Q}_{rem} , calculated at step 4 is specified as a volumetric heat sink for the fluid region corresponding to the flue gases/helium heat exchanger (Fig. 4), thus cooling down the flue gases crossing such fluid region accordingly.

Table 3

Solution uncertainty and Grid Convergence Index for the fine, base and coarse computational grids.

Mesh	Elements	U_{sver} (%)	GCI (%)
Coarse	270,000	7	9
Base	382,000	5	7
Fine	550,000	4	5

Regarding the other boundary conditions, standard wall functions are used at the walls and symmetry conditions are applied to the planes delimiting the modeled angular sector.

4.3. Physical models

Favre-averaged Navier–Stokes equations are solved across the computational domain, using the standard $k-\epsilon$ turbulence model for Reynolds stresses. Following the results obtained in previous studies on the mathematical modeling of flameless combustion [19–21], the Eddy Dissipation Concept (EDC) [22,23] model is taken into account for turbulence chemistry-interactions, to capture the volumetric features of the investigated combustion regime. The effect of the kinetic mechanism on the results is investigated, comparing the results provided by a global kinetic approach and a detailed kinetic scheme. The 4-step global kinetic scheme by Jones and Lindstedt [24] is used for both methane and hydrogen-enriched fuels. This scheme will be denoted as JL. The detailed scheme is the so-called KEE-58 [25], which involves 17 species in 58 reversible reactions.

As far as NO formation is concerned, only thermal and prompt NO formation are considered, due to the relatively high process temperatures observed experimentally, which make the contributions of other routes, i.e. N_2O [26] and NNH [27–29], negligible, as shown in [21]. Thermal NO formation is modeled with a simplified one-step kinetic mechanism, available in the code [30] and obtained from the reduction of the full Zeldovich scheme by assuming a steady state for the N radicals and relating the O radical concentration to that of oxygen by means of the dissociation reaction. The prompt NO formation from methane is modeled using a similar approach, according to the one-step mechanism proposed by [31]. For both thermal and prompt NO formations, the Arrhenius equation is integrated over a probability density function (PDF) for temperature, to account for turbulence effects.

Finally, radiation modeled with the P_1 radiation model, based on the expansion of the radiation intensity into an orthogonal series of spherical harmonics [32]. The P_1 model can provide reasonable results when radiation is emitted isotropically, as it happens for combustion applications. The Weighted-Sum-of-Gray-Gases (WSGG) model is used for predicting the spectral properties [33].

The influence of molecular diffusion has been also considered. Binary diffusion coefficients are calculated following the kinetic theory and a modification of the Chapman–Enskog formula [34]. Then, an effective diffusion coefficient of the species in the mixture is obtained by applying the Wilke's mixing rule [35].

5. Results

The results of the numerical modeling on the CHP flameless are shown here. First, the main features of the flow field inside the combustion chamber are presented. Then, the effect of the kinetic mechanism adopted for gas-phase oxidation is analyzed, followed by a discussion regarding the influence of hydrogen addition to the structure of the reaction zone in the combustion chamber. Finally, the validation of the computational approach is shown, comparing the numerical results with the available experimental data.

5.1. Flow field and main operating features

The analysis of the flow field in the combustion chamber indicates that the flue gases are entrained into the flame tube by the high velocity air jet. Fuel is also entrained by air and mixed with flue gas stream. The recirculation degree in the combustion chamber can be determined as:

$$k_R = \frac{\dot{m}_{fg,R}}{(\dot{m}_{fuel} + \dot{m}_{air})} \quad (3)$$

where $\dot{m}_{fg,R}$ is the mass flow rate of the exhaust gases recirculating into the reaction zone, whereas \dot{m}_{fuel} and \dot{m}_{air} represent the fuel and air mass flow rates fed to the burner. The values of k_R obtained for the different runs are listed in the second column of Table 4: the burner generates a degree of recirculation, i.e. 106–112%. The average conditions in terms of oxygen availability (Column 3, Table 4), and temperature, T_m (Column 4, Table 4), after the flue and fresh gas mixing process, are approximately $Y_{O_2,m} = 0.15$ and $T_m = 1240$ K, respectively. Therefore, recirculation allows achieving both dilution and preheating of the reactants, required to operate in flameless regime. The fifth column in Table 4 lists the maximum temperature increase observed for the different investigated runs, as provided by the KEE-58 kinetic mechanism. Following the criterion of Cavaliere and de Joannon [7], the burner operates in flameless mode only when fed with CH_4 , being the observed ΔT_{max} below the fuel self-ignition temperature (i.e. 853 K). When hydrogen is added to the fuel, the self-ignition temperature is in between that of hydrogen (i.e. 783 K) and that of methane (i.e. 853 K). In such cases the observed ΔT_{max} values are higher, i.e. ~1020–1050 K, thus indicating a strong effect of hydrogen reactivity on the flame structure. Therefore, the system operation cannot be strictly regarded as flameless and higher recirculation degrees should be ensured when operating with hydrogen-

based fuels. The last column in Table 4 reports the ratio $\dot{W}_{el}/\dot{Q}_{rem}$ obtained from the numerical simulations, using the user-defined function described in Section 4.2. Such ratio is related to the thermal efficiency of the Stirling cycle by the regenerator efficiency:

$$\eta_{th,St} = \frac{\dot{W}_{el}}{\dot{Q}_{rem} + (1 - \eta_{reg})\dot{Q}_{reg}} \quad (4)$$

where \dot{Q}_{rem} and η_{reg} are the heat supplied to the working fluid in the regenerator and the regenerator efficiency, respectively. In real life operation, η_{reg} is smaller than 1 and, therefore, the thermal Stirling efficiency, $\eta_{th,St}$ will be lower than the ratio $\dot{W}_{el}/\dot{Q}_{rem}$. The experimental measurements collected in the present investigation do not allow the calculation of \dot{Q}_{rem} and the estimation of η_{reg} . However, the measured $\dot{W}_{el}/\dot{Q}_{rem}$ ratios (column 6 in Table 4), in the range 0.44–0.48, result compatible with the expected performances of a Stirling engine with regenerator, which are reported to be in the range 35–40%. Such result can be considered as a first validation, of the model adopted to replace the explicit operation of the finned helium/flue gases heat exchanger.

5.2. Effect of the kinetic mechanism on the flame structure

Fig. 6 shows the contour plots of temperature inside the combustion chamber fed with CH_4 , at a helium pressure, $P_{He} = 90$ bar, predicted by the EDC model with the JL (a) and KEE-58 (b) kinetic mechanisms. A major influence of the kinetic scheme on the structure of the reaction zone is observed. The global chemistry approach results in a flame shape characteristic of a non-premixed flame with a thin flame front and high temperature peaks along the burner axis. Conversely, when the KEE-58 scheme is employed, the reaction region is fully detached from the burner nozzles and shifted along the axis, towards the closed end of the combustion chamber. Moreover the temperature distribution in the flame tube is much more uniform and the maximum predicted temperature, i.e. 2050 K, is significantly smaller than that provided by the 4-step (JL) mechanism, i.e. 2585 K.

Run	k_R (%)	$Y_{O_2,m}$ (-)	T_m (K)	ΔT_{max} (K)	$\dot{W}_{el}/\dot{Q}_{rem}$ (-)
1	107	0.15	1231	817	0.45
2	110	0.15	1234	1057	0.48
3	112	0.16	1251	1059	0.47
4	106	0.14	1196	675	0.44
5	108	0.16	1203	1016	0.47
6	109	0.16	1205	1022	0.46

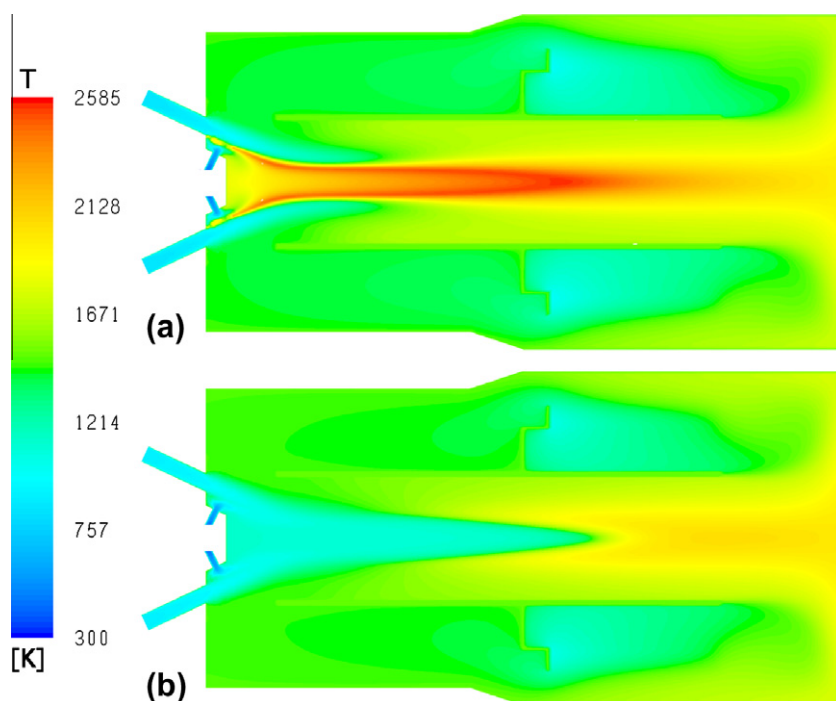


Fig. 6. Temperature distribution in the combustion chamber fed with CH_4 , predicted by the JL (a) and KEE-58 (b) kinetic mechanisms. $P_{He} = 90$ bar. Run 1, Table 1.

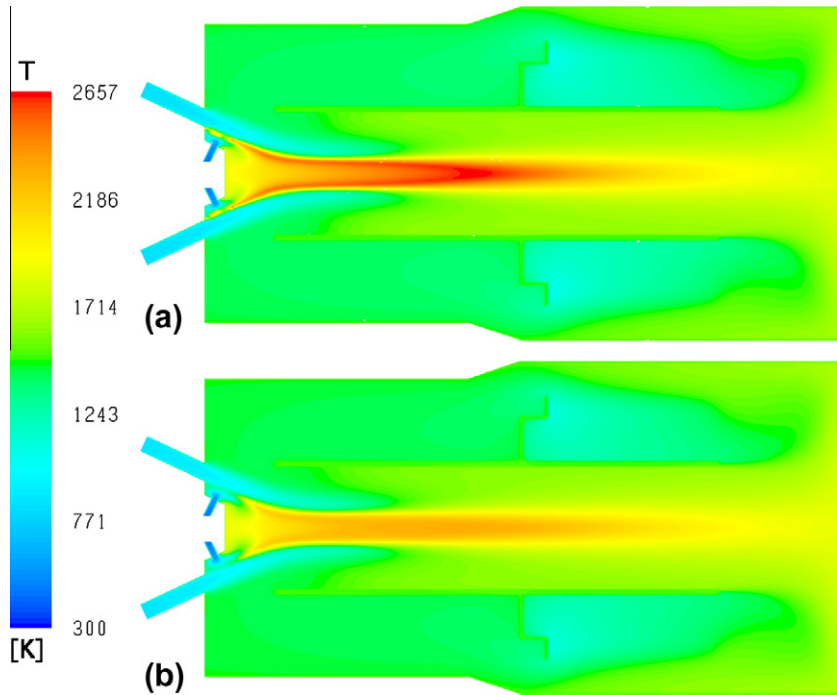


Fig. 7. Temperature distribution in the combustion chamber fed with CH_4/H_2 (H_2 9% by wt.) predicted by the JL (a) and KEE-58 (b) kinetic mechanisms. $P_{\text{He}} = 90$ bar. Run 1, Table 1.

Fig. 7 illustrates the temperature distribution in the combustion chamber fed with a CH_4/H_2 mixture containing 9% (by wt.) of H_2 , at a helium operating pressure $P_{\text{He}} = 90$ bar. When hydrogen is added to the fuel, the qualitative differences between the results provided by the JL and KEE-58 kinetic mechanism are smaller. Both schemes indicate the ignition of the fuel mixture in the region immediately downstream the fuel injection nozzles, with a defined flame region developed along the burner axis. However, the results provided by KEE-58 indicate a more diffuse reaction zone, without the thin

flame sheets characterizing the temperature distribution predicted by the global approach. Finally, the temperature levels are significantly lower with KEE-58, being the maximum predicted temperature, i.e. 2309 K, approximately 350 K lower than that obtained with the JL mechanism.

Such considerations are quantitatively supported by the analysis of the radial profile of temperature provided by the JL and KEE-58 mechanisms, shown in **Fig. 8** for different axial locations, i.e. $x = 0.075$ m (a), $x = 0.150$ m (b), $x = 0.250$ m (c) and $x = 0.350$ m (d).

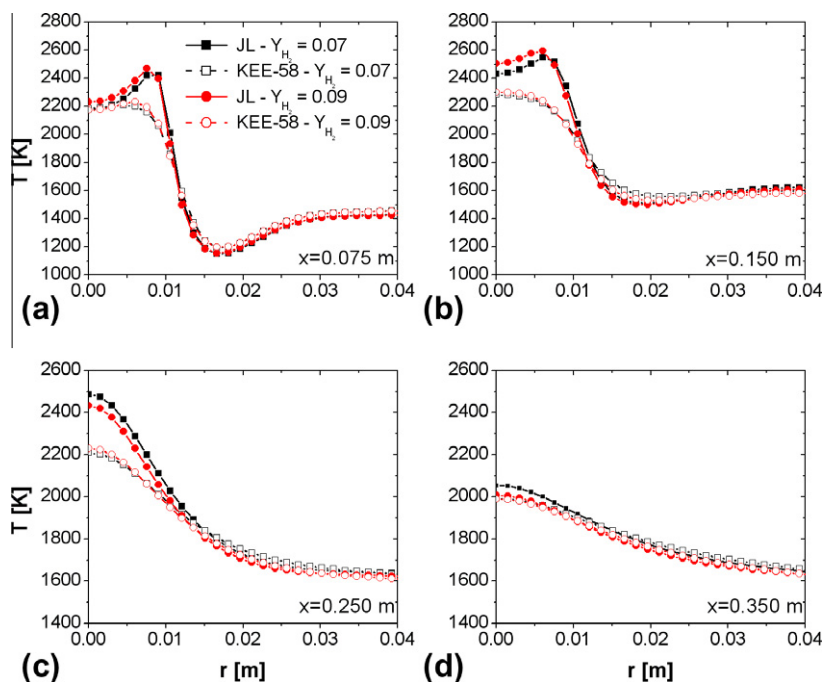


Fig. 8. Radial temperature profiles at different axial locations, i.e. $x = 0.075$ m (a), $x = 0.150$ m (b), $x = 0.250$ m (c) and $x = 0.350$ m (d), predicted by the JL (JL) and KEE-58 mechanisms for a hydrogen content in the fuel equal to 7% and 9% (by wt.), respectively. $P_{\text{He}} = 90$ bar. Runs 2 and 3, Table 1.

Two cases, corresponding to 7% and 9% H₂ mass fractions are considered, at a helium pressure $P_{\text{He}} = 90$ bar. The profiles provided by the global chemistry approach not only indicate higher temperature levels with respect to KEE-58, but they also show a different flame structure. With KEE-58, the temperature distribution in the high temperature region ($x = 0.075$ m and $x = 0.150$ m) is always flatter than that obtained with the JL scheme, which provides more pronounced peaks indicating the existence of a thin diffusive flame front (Fig. 8a and b). When the distance from the burner is increased ($x = 0.250$ m and $x = 0.350$ m), the profiles obtained with the two approaches are qualitatively very similar, although global chemistry results in higher temperatures.

5.3. Effect of H₂ addition to the fuel

Fig. 9 shows the effect of hydrogen addition, i.e. 0 (a), 7 (b) and 9 (c) % (by wt.), on the flame structure in the combustion chamber, at a helium pressure $P_{\text{He}} = 90$ bar. Hydrogen has a significant impact on the radical pool and, then, it directly affects the ignition process. For the methane case (Fig. 9a), the oxidation occurs close to the exit section of the flame tube, with a homogeneous temperature distribution. When hydrogen is added to the fuel (Fig. 9b and c), the ignition zone is shifted backward and a well-defined high temperature region is observed. Moreover, the flame becomes shorter and thinner, when increasing the H₂ mass fractions. The visual evi-

dence provided by Fig. 9 supports the conclusions suggested by the ΔT_{max} values, discussed in Section 5.1. When H₂ is added to the fuel, a homogeneous temperature distribution is no longer observed in the combustion chamber, being the effect of hydrogen reactivity dominant with respect to flue gas dilution. A possible solution to such problem could imply the modification of the burner feeding system, to attain higher values of k_R within the combustion chamber.

5.4. Effect of burner load

Fig. 10 shows the radial temperature profiles obtained at different axial locations, i.e. $x = 0.075$ m (a), $x = 0.150$ m (b), $x = 0.250$ m (c) and $x = 0.350$ m (d), when increasing the H₂ mass fraction in the fuel, for two different helium pressures, $P_{\text{He}} = 90$ and 120 bar, corresponding to burner loads of ~ 24 and ~ 30 kW, respectively. Fig. 10 quantitatively confirms the effect of hydrogen on fuel ignition, as discussed in Section 5.4. Regarding the comparison between the different operating pressures, it could appear unexpected that the lower burner load results in higher temperature levels, especially closer to the burner (Fig. 10a and b). However, such behavior can be easily explained by taking into account that the burner is designed for the highest load, so that the internal fluid dynamic is optimized for such conditions; when operating with reduced flow rates, ignition occurs before the fresh

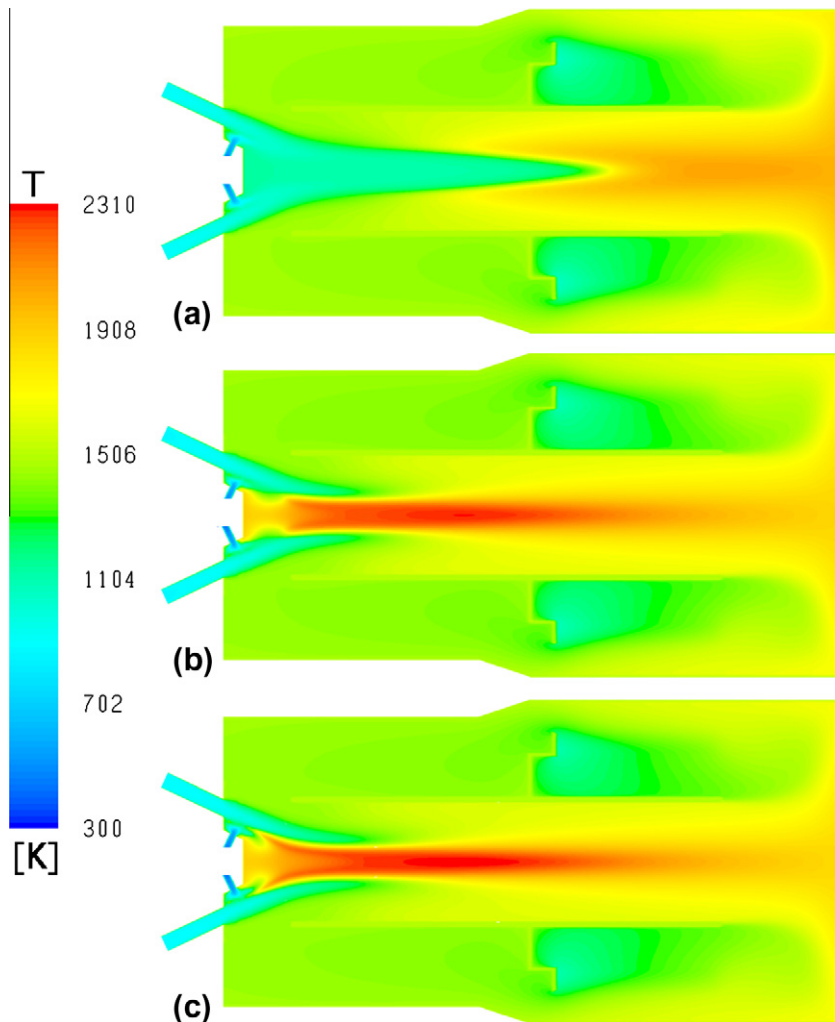


Fig. 9. Temperature distribution in the combustion chamber fed with mixtures containing 0 (a), 7 (b) and 9 (c) % (by wt.) of H₂, predicted by the KEE-58 kinetic mechanism. $P_{\text{He}} = 90$ bar. Runs 2 and 3, Table 1.

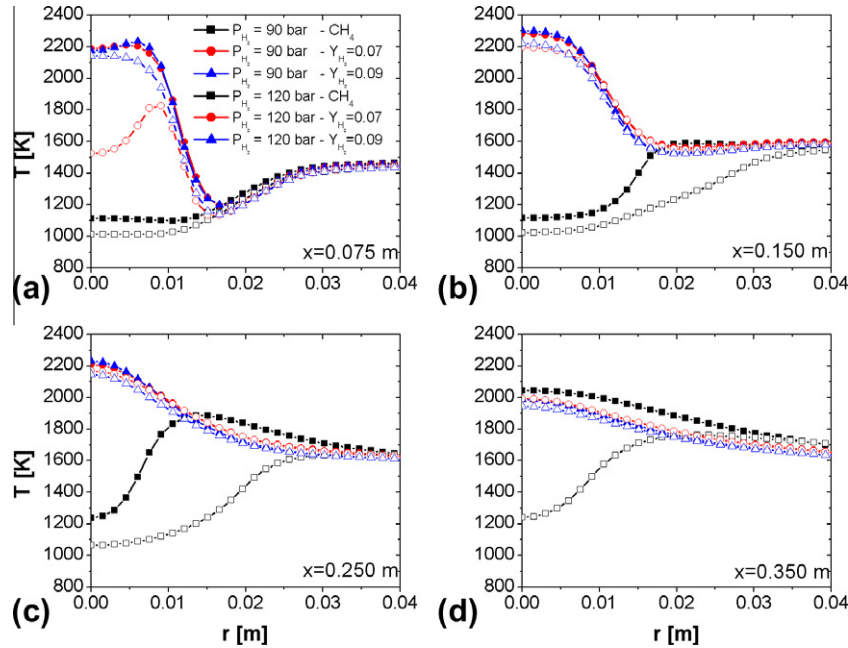


Fig. 10. Radial temperature profiles at different axial locations, i.e. $x = 0.075$ m (a), $x = 0.150$ m (b), $x = 0.250$ m (c) and $x = 0.350$ m (d), predicted by the KEE-58 kinetic mechanism for a H_2 content in the fuel equal to 0%, 7% and 9% (by wt.), respectively. $P_{\text{He}} = 90$ and 120 bar. Runs 1–6, Table 1.

gases have entrained a sufficient amount of flue gases, thus resulting in higher temperature peaks. Fig. 10 also points out that the reaction zone is shifted towards the end of the flame tube for the CH_4 fuel case. For $P_{\text{He}} = 90$ bar, the reaction region is collocated between $x = 0.250$ m (Fig. 10c) and $x = 0.350$ m (Fig. 10d), as indicated by the temperature rise at the axis, from about 1250 K to approximately 2050 K. On the other hand, for the $P_{\text{He}} = 120$ bar case, no ignition is observed up to an axial distance of $x = 0.350$ m (Fig. 10d), the temperature profile simply increasing from the mixed temperature value, T_m (Column 4, Table 4) to the flame tube temperature. Then, the reaction zone is shifted further towards the closed end of the combustion chamber with respect to the $P_{\text{He}} = 90$ bar case.

5.5. Model validation

A first validation of the modeling approach has been already provided in Section 5.1, being the estimated heat flux to the working fluid of the Stirling engine compatible with the values of thermal efficiencies found in the literature for similar systems [36].

The present section provides a comparison between predicted and measured CO and NO emissions from the unit. Following Oberkampf and Barone [37] and Parente et al. [38], the error associated to the numerical simulations, \tilde{E} , and the related confidence, Cl , are determined:

$$\tilde{E} = (y_m - \bar{y}_e) \pm Cl \quad (5)$$

$$Cl = \bar{y}_e \pm \sqrt{\left(t_{\alpha/2,v} \frac{s}{\sqrt{n}} \right)^2 + U_e^2} \quad (6)$$

where y_m and \bar{y}_e represent the model output and the measured value, respectively and n is the number of experimental replicates. The terms under the square root in Eq. (6) represent the two contributions to the global uncertainty, the statistical reproducibility and the experimental error, respectively. The first term is calculated assuming that the measurements follow a t -student distribution: $t_{\alpha/2,v}$ is the quantile of the measured population with $v = n - 1$ de-

grees of freedom, s is the sample standard deviation and α is the desired level of confidence. The experimental uncertainty, U_e , is obtained from the literature. Following Gluck et al. [39] and Mounaud [40], relative errors of 5% and 3% have been assumed for the measurements of NO and CO, carried out with the Siemens ULTRAMAT 6 analyzer.

Global metrics can be also provided to summarize the performances of the two kinetic mechanisms for the two investigated pressure levels, $P_{\text{He}} = 90$ and 120 bar. In particular, an average error metric and confidence interval can be defined:

$$\left| \frac{\tilde{E}}{\bar{y}_e} \right|_{avg} = \frac{1}{p} \sum_{i=1}^p \left| \frac{\tilde{E}_i(x_i)}{\bar{y}_e(x_i)} \right| \left| Cl \right|_{avg} = \frac{1}{p} \frac{t_{\alpha/2,v}}{\sqrt{n}} \sum_{i=1}^p \left| \frac{s_i(x_i)}{\bar{y}_e(x_i)} \right| \quad (7)$$

Fig. 11 shows the comparison between measured and calculated CO (a) and NO (b) emissions from the combustion chamber, with the different kinetic mechanisms adopted. It is very clear that the global kinetic approach results in major discrepancies for both CO and NO values, indicating its inadequacy to properly describe the oxidation process; in particular, the large NO emissions reflect a non negligible over prediction of the temperature levels by the JL scheme, as already discussed in Section 5.3. With regard to the KEE-58 kinetic mechanism, a very good agreement with the experimental data is observed for the $P_{\text{He}} = 90$ bar case. An excellent quantitative agreement is observed for both NO and CO emissions, as confirmed by Table 5. The average error metrics are $12\% \pm 7\%$ and $14\% \pm 16\%$ for NO and CO, respectively, with 95% confidence. The higher confidence interval, i.e. 16%, for the CO case reflects the strong variations observed for such chemical species during the experimental campaign. Such level of predictivity is extremely satisfying, especially if we take into account the absolute values of the monitored output variables: CO and NO ranges are between 6–12 ppm_v and 46–51 ppm_v, respectively. This means that absolute errors in the predictions of a few ppm may lead to large errors when normalized to the measured value. The level of agreement provided by the KEE-58 mechanism is less satisfactory for the $P_{\text{He}} = 120$ bar, especially for the NO emissions, which are under predicted over the entire range of the H_2 mass fractions. The average error metrics (Table 5) for NO and CO are $58\% \pm 6\%$

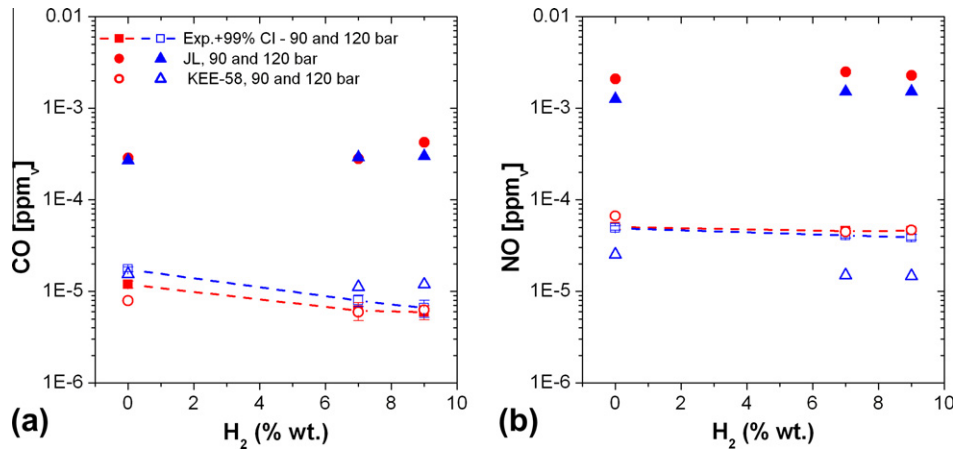


Fig. 11. Relative and global validation metrics for NO and CO measurements (dry basis) at different burner loads, obtained with the JL and KEE-58 kinetic mechanisms. Runs 1–6, Table 1.

Table 5

Comparison between predicted and experimental NO and CO emissions (dry basis).

Run	CO				NO			
	Model (ppm _v)		Exp (ppm _v)		$\tilde{E} = (y_m - \bar{y}_e)/\bar{y}_e $		Cl/\bar{y}_e	
	JL	KEE	JL	KEE	JL	KEE	JL	KEE
1	284	7.9	12.0	23.0	0.33	0.09	2090	66.7
2	280	5.9	6.2	44.5	0.04	0.22	2480	44.7
3	423	6.3	5.9	70.3	0.06	0.18	2270	46.8
4	268	15.4	17.4	14.4	0.12	0.06	1260	25.2
5	291	11.2	7.9	35.7	0.41	0.14	1510	15.0
6	300	11.9	6.6	44.6	0.81	0.21	1520	14.7
$ \tilde{E}/\bar{y}_e _{avg}$								
P_{He} (bar)		JL	KEE	$ Cl/\bar{y}_e _{avg}$		$ \tilde{E}/\bar{y}_e _{avg}$		$ Cl/\bar{y}_e _{avg}$
90		45.9	0.14	0.16		47.5		0.07
120		31.6	0.45	0.14		32.9		0.06

and $45\% \pm 14\%$ respectively, thus indicating a significant departure from the experimental data. Indeed, results provided by KEE-58 show a strong improvement with respect to the global chemistry approach, which provides CO and NO values higher than the measured ones by more than a order of magnitude (Table 5). The poor performance of KEE-58 for the $P_{He} = 120$ bar case with respect to the $P_{He} = 90$ bar is probably related to the strong approximation made for estimating the air inlet temperature (Section 4.2). The preheating efficiency can be significantly affected by the operating conditions, i.e. flow rates, and considering an average value of 0.5 can be inappropriate in some cases, especially at the higher loads, when the pre-heater is expected to perform better. Therefore, it would be desirable to get directly such temperature from the experimental measurements, to avoid the consequences of such rough approximation. To this purpose, three additional thermocouples have been placed near the air inlet section for the future experimental campaigns.

6. Conclusions

The present paper presents a numerical and experimental investigation of a micro-CHP unit, equipped with a flameless burner which supplies the heat required by a Stirling engine for the production of electrical power. The activity has been focused on the effect of adding hydrogen to the fuel on the combustion regime features and, thus, to assess the feasibility of flameless combustion with hydrogen-enriched fuels.

The numerical model of the combustion chamber helped understanding observed results and gaining considerable insight into the combustion features; however its development required significant efforts.

Firstly, geometrical features of the combustion chamber lead to a quite heavy computational grid, although some details were neglected by using appropriate procedures (e.g. the heater with finned surface was simulated as an heat sink). Secondly, proper boundary conditions had to be defined in order to correctly couple the oxidation process to the overall operation of the CHP unit. In particular, the knowledge of the heat transferred to the working fluid of the Stirling cycle was required to properly reproduce the energy balance of the system. To this purpose, a user-defined subroutine was developed to evaluate such energy flux, based on information provided by the experimental campaign, i.e. burner load, and by the numerical simulation itself, i.e. exhaust temperature and air inlet temperature. The external subroutine proved to perform satisfactory, providing values of the heat source for the Stirling cycle which lead to expected thermal efficiencies in agreement with those indicated in the literature for similar systems.

Finally, rather detailed kinetic schemes were needed to capture flameless combustion, global schemes leading to unrealistic temperature and emission levels.

Regarding the main features of the combustion process, results showed more uniform temperature distribution in the combustion chamber for the higher loads, being the system designed to optimize the mixing process for such operating conditions. The addition of hydrogen to the fuel was found to deeply affect the flame

structure, resulting in a reaction region progressively shifted towards the burner for increasing H₂ values. Moreover, the temperature distribution with hydrogen-enriched fuels evidenced the existence of a hot core, characterized by steep gradients, indicating operation in an intermediate regime between flameless oxidation and a conventional diffusion flame.

The comparison between the predicted and measured NO emissions indicated a very good quantitative agreement for the medium burner loads, whereas NO emissions at full load were under predicted, although the experimental trend was well captured. The reason for such inaccuracies are mainly to be found in the large uncertainty related to the estimation of the air inlet temperature, which directly affects the temperature increase due to the oxidation process and ultimately influences the energy balance performed by the user-defined subroutine. Following such considerations, a new experimental campaign has been planned after a modification of the experimental apparatus, in order to measure directly the air temperature after preheating.

Acknowledgements

We would like to acknowledge Ing. Silvia Soricetti from ENEL Energia e Innovazione S.p.A. who took part in the experimental activity.

References

- [1] Onovwiona HI, Ugursal VI. Residential cogeneration systems: review of the current technology. *Renew Sustain Energy Rev* 2006;10:389–431.
- [2] Onovwiona HI, Ugursal VI, Fung AS. Modeling of internal combustion engine based cogeneration system for residential applications. *Appl Therm Eng* 2007;27:848–61.
- [3] Pehnt M. Environmental impacts of distributed energy system – the case of micro cogeneration. *Environ Sci Policy* 2008;11:25–37.
- [4] Thomas B. Benchmark testing of Micro-CHP units. *Appl Therm Eng* 2008;28:2049–54.
- [5] www.cleanenergyindustries.com.
- [6] Wünnig JA, Wünnig JG. Flameless oxidation to reduce thermal NO-formation. *Prog Energy Combust Sci* 1997;23:81–94.
- [7] Cavaliere A, de Joannon M. Mild combustion. *Prog Energy Combust Sci* 2004;30:329–66.
- [8] Weber R, Smart JP, vd Kamp W. On the (MILD) combustion of gaseous, liquid, and solid fuels in high temperature preheated air. *Proc Combust Inst* 2005;30:2623–9.
- [9] Gupta AK. Thermal characteristics of gaseous fuel flames using high temperature air. *J Eng Gas Turb Power* 2004;126:9–19.
- [10] Tsuji H, Gupta AK, Hasegawa T, Katsuki M, Kishimoto K, Morita M. High temperature air combustion: from energy conservation to pollution reduction. Boca Raton, Florida: CRC Press; 2003.
- [11] M. Katsuki, T. Hasegawa, The science and technology of combustion in highly preheated air. In: Symposium (International) on combustion. vol. 27; 1998. p. 3135–46.
- [12] Derudi M, Villani A, Rota R. Mild combustion of industrial hydrogen containing byproducts. *Ind Eng Chem Res* 2007;46:6806–11.
- [13] Sabia P, de Joannon M, Fierro S, Tregrossi A, Cavaliere A. Hydrogen enriched methane mild combustion in a well stirred reactor. *Exp Therm Fluid Sci* 2007;31:469–75.
- [14] Medwell PR, Kalt PAM, Dally BB. Simultaneous imaging of OH, formaldehyde, and temperature of turbulent nonpremixed jet flames in a heated and diluted coflow. *Combust Flame* 2007;148:48–61.
- [15] Medwell PR, Kalt PAM, Dally BB. Imaging of diluted turbulent ethylene flames stabilized on a jet in Hot Coflow (JHC) burner. *Combust Flame* 2008;152:100–13.
- [16] Logan RW, Nitta CK. Comparing 10 methods for solution verification, and linking to model validation. *J Aero Comput Inform Comm* 2006;354–73.
- [17] Roache PJ. Verification and validation in computational science and engineering. Albuquerque, NM: Hermosa Publishers; 1998.
- [18] Kee RJ, Rupley F, Miller JA. The CHEMKIN thermodynamic data base. Report SAND89-8008. Livermore, CA: Sandia National Laboratories; 1989.
- [19] Christo FC, Dally BB. Modelling turbulent reacting jets issuing into a hot and diluted coflow. *Combust Flame* 2005;142:117–29.
- [20] Parente A, Galletti C, Tognotti L. Effect of the combustion model and kinetic mechanism on the MILD combustion in an industrial burner fed with hydrogen enriched fuels. *Int J Hydro Energy* 2008;33:7553–64.
- [21] Galletti C, Parente A, Derudi M, Rota R, Tognotti L. Numerical and experimental analysis of NO emissions from a lab-scale burner fed with hydrogen-enriched fuels and operating in MILD combustion. *Int J Hydro Energy* 2009;34:8339–51.
- [22] Magnussen B, Hjertager B. On mathematical modeling of turbulent combustion with special emphasis on soot formation and combustion. *Proc Combust Inst* 1977;16:719–29.
- [23] Gran IR, Magnussen BF. A numerical study of a bluff-body stabilized diffusion flame. Part 2. influence of combustion modeling and finite-rate chemistry. *Combust Sci Technol* 1996;119:191–217.
- [24] Jones WP, Lindstedt RP. Global reaction schemes for hydrocarbon combustion. *Combust Flame* 1988;73:233–49.
- [25] Bilger R, Starner S, Kee R. On reduced mechanisms for methane-air combustion in nonpremixed flames. *Combust Flame* 1990;80:135–49.
- [26] Malte P, Pratt D. Measurement of atomic oxygen and nitrogen oxides in jet-stirred combustion. *Proc Combust Inst* 1975;15:1061–70.
- [27] Bozzelli JW, Dean AM. O + NHH – a possible new route for NO_x formation in flames. *Int J Chem Kinet* 1995;27:1097–109.
- [28] Hayhurst AN, Hutchinson EM. Evidence for a new way of producing NO via NHH in fuel-rich flames at atmospheric pressure. *Combust Flame* 1998;114:274–9.
- [29] Konnov AA, Colson G, Ruyck JD. NO formation rates for hydrogen combustion in stirred reactors. *Fuel* 2001;80:49–65.
- [30] Flueni 6.3 User Guide.
- [31] De Soete GG. Overall reaction rates of NO and N₂ formation from fuel nitrogen. *Proc Combust Inst* 1974;15:1093–102.
- [32] G.D. Raithby, Equations of motion for reacting, particle-laden flows. Tech. Rep. Thermal Science Ltd.; 1991.
- [33] Smith TF, Shen ZF, Friedman JN. Evaluation of coefficients for the weighted sum of gray gases model. *J Heat Trans* 1982;104:602–8.
- [34] McGee HA. Molecular engineering. New York, NY: McGraw-Hill; 1991.
- [35] Wilke SP. A viscosity equation for gas mixtures. *J Chem Phys* 1950;18:517–9.
- [36] Timoumi Y, Tili I, Nasrallah SB. Performance optimization of Stirling engines. *Renew Energy* 2008;33:2134–44.
- [37] Oberkampf WL, Barone MF. Measures of agreement between computation and experiment: validation metrics. *J Comput Phys* 2006;217:5–38.
- [38] Parente A, Galletti C, Tognotti L. A simplified approach for predicting NO formation in MILD combustion of CH₄–H₂ mixtures. *Proc Combust Inst* 2011;33:3343–50.
- [39] Gluck S, Glenn C, Logan T, Vu B, Walsh M, Williams P. Evaluation of NO_x flue gas analyzers for accuracy and their applicability for low-concentration measurements. *J Air Waste Manage Assoc* 2003;53:749–58.
- [40] G. Mounaud, A parametric study of the effect of fire source elevation in a compartment. MSc thesis in Mechanical Engineering. Faculty of the Virginia Polytechnic Institute and State University; 2004.